Statewide Real-time Quantitative Precipitation Estimation Using Weather Radar and NWP Model Analysis: Algorithm Description and Product Evaluation

Bong-Chul Seo and Witold F. Krajewski

IIHR—Hydroscience & Engineering, The University of Iowa, Iowa City, IA 52242, USA

Revised Manuscript Submitted to

Environmental Modelling & Software

June 2020

Corresponding author address: Bong-Chul Seo, IIHR—Hydroscience & Engineering, The University of Iowa, Iowa City, IA 52242, USA.
Email: bongchul-seo@uiowa.edu

ABSTRACT

This study describes an automated system that generates a statewide real-time quantitative precipitation estimation (QPE) product for flood forecasting in Iowa. The QPE system is comprised of real-time data acquisition, processing, and product visualization subsystems. Combined with information retrieved from numerical weather prediction, the system processes data from multiple radars using various algorithms accounting for precipitation microphysics and radar remote sensing uncertainties. The system generates a composite rainfall map covering the entire state of Iowa at a resolution of 0.5 km, updated every five minutes. With the help of the system's flexible modular configuration, we have recently added a new polarimetric algorithm based on specific attenuation. Independent evaluations based on comparisons with rain gauge data and hydrologic model prediction of streamflow demonstrate that the new implementation significantly improves the rainfall estimation accuracy. The new QPE product shows performance comparable to the Multi-Radar Multi-Sensor product that contains a rain gauge correction.

Keywords: QPE, Radar, Rainfall, Flood forecasting, Specific attenuation

1. Introduction

Using data from the U.S. Weather Surveillance Radar-1988 Doppler (WSR-88D) network, the Iowa Flood Center (IFC) has provided a statewide real-time rainfall product since the IFC's establishment in 2009. This product generation was motivated by the need for real-time flood prediction in Iowa, which has repeatedly experienced devastating floods at various scales in recent decades (e.g., Smith et al., 2013; Vennapusa and White, 2015; Seo et al., 2018). Our goal to forecast "everywhere" and cover all Iowa communities (e.g., regardless of catchment scale) has led to the use of a distributed hydrologic model, which requires spatially variable rainfall inputs (Krajewski et al., 2017).

The IFC quantitative precipitation estimation (QPE) framework was initially built on the real-time Hydro-NEXRAD application (Krajewski et al., 2011; Kruger et al., 2011; Seo et al., 2011; Krajewski et al., 2013). Most scientific algorithms in our QPE system have evolved according to the WSR-88D's hardware and polarimetric upgrades (e.g., Istok et al. 2009). The IFC QPE system acquires real-time data from seven WSR-88Ds (KARX in La Crosse, Wisconsin; KDMX in Des Moines, Iowa; KDVN in Davenport, Iowa; KEAX in Kansas City, Missouri; KFSD in Sioux Falls, South Dakota; KMPX in Minneapolis, Minnesota; and KOAX in Omaha, Nebraska), as shown in Fig. 1. The system then generates a composite rain rate map covering the entire domain (Fig. 1), with temporal and spatial resolutions of five minutes and 0.5 km, respectively, using a variety of processing algorithms, as documented in Seo et al. (2011; 2015) and Seo and Krajewski (2015).

As of early 2019, we had added a state-of-the-art polarimetric algorithm known as "specific attenuation" (e.g., Ryzhkov et al., 2014; Wang et al., 2019) to our QPE procedures to fully benefit from the WSR-88D's dual-polarization (DP) capability. This new

algorithm required several new elements; for example, one that retrieves temperature soundings from the numerical weather prediction (NWP) model analyses to identify the melting layer (ML) location. Before this new implementation, the use of DP in the IFC system was limited to basic data quality control (e.g., removal of non-meteorological returns), and the system's main estimator was a single polarization–based algorithm using a reflectivity-rain rate (*Z-R*) relation. The new implementation using the specific attenuation method promises to be the most significant milestone in our system's 10-year history, as the method has demonstrated meaningful improvements in QPE accuracy (Seo et al., 2020b).

Therefore, we take this opportunity to document the architecture and capabilities of our fully automated QPE system, including algorithm updates and new developments as well as the way it complements the outdated descriptions presented in Seo et al. (2011). To validate the attainable improvement in QPE and subsequent hydrologic prediction, we generated the statewide QPE products using the latest and prior algorithms for a three-year period (2016–2018) and evaluate the performance of each one using rain and stream gauge observations. We also compared the performance of our QPE products with that of U.S. national QPE products (e.g., Zhang et al., 2016; Cunha et al., 2013) that have been widely used for meteorological and hydrological applications.

In Section 2, we describe the architecture of our QPE system by specifying the three main subsystems associated with real-time data acquisition, NWP analysis and radar data processing, and final product visualization. Section 3 provides the algorithm details of module elements in the NWP, individual radar, and composite data processing. Section 4 evaluates the QPE products generated by our algorithms using rain gauge data and

hydrologic simulations. In Section 5, we summarize the algorithm features and main findings from the product evaluation. Finally, we discuss the improvements gained by implementing the new polarimetric algorithm and potential future developments.

2. System architecture

A real-time QPE system requires several modular elements, ranging from data acquisition to final product generation. These modules include real-time radar and NWP data retrieval, algorithms for data quality control, volume scan data processing and precipitation estimation, and digital product and statewide map generation. Our QPE system comprises three main subsystems: (1) the Local Data Manager (LDM; e.g., Fulker et al., 1997) system for real-time NWP analysis and radar data acquisition; (2) the data processing system that contains a variety of scientific algorithms associated with precipitation estimation as illustrated in Fig. 2; and (3) the product visualization system for weather monitoring.

2.1 Local Data Manager

The IFC LDM system acquires real-time streaming Level II radar volume data (e.g., Crum et al., 1993; Kelleher et al., 2007) and NWP model analyses using Internet Data Distribution (IDD) technology (Yoksas et al., 2006). Level II data containing six radar observables (reflectivity, radial velocity, spectrum width, differential reflectivity, copular correlation coefficient, and differential phase) are split into multiple files (usually more than 100 for a single volume scan) and then distributed for faster data transfer. Once our LDM has confirmed receipt of all the radar volume file pieces labelled with sequential integers, it combines them and performs a basic quality check (e.g., counting the number

of elevation angles) for file completeness. More detailed descriptions of the Level II data reception, quality check, data packing, and format conversion are documented in Krajewski et al. (2013).

We also obtain analysis results of temperature and geopotential height at various pressure levels (e.g., between 100 and 1,000 mb) and at ground level (e.g., 2 m above) from the Rapid Refresh (RAP) and High-Resolution Rapid Refresh (HRRR) models (e.g., Weygandt et al., 2009; Benjamin et al., 2016). RAP and HRRR are continental-scale, real-time convection-allowing models updated hourly with 13 and 3 km resolution horizontal grids, respectively. The HRRR model is fully dependent on its parent models, the radar-assimilating RAP and the radar-enhanced Rapid Update Cycle (RUC). The atmospheric variables we retrieve from the two NWP models are not model forecasts, but rather the model analysis used for model initializations. We use the retrieved NWP variables to build the information required for precipitation classification (e.g., rain/snow) and ML identification, which can significantly affect the accuracy of radar-derived QPE. Since the latency of this NWP analysis through LDM can be up to two hours (based on our several years of operational experience), we assume that the retrieved NWP variables (e.g., temperature and geopotential height) do not change substantially over this time.

2.2 Data processing

This subsystem includes processing algorithm modules for radar data quality control, precipitation estimation and correction, map coordinate transformation, and precipitation product generation. As illustrated in Fig. 2, the system manager (i.e., Python scripts) sequentially executes the algorithm modules and organizes the input and output data of each sequential procedure. We use the NASA Radar Software Library, an object-oriented

library written in C, to decode radar Level II data. Our algorithm modules are also written in C for compatibility and efficient data processing. The key feature of the data processing system is its modular algorithm structure, which makes it easier to upgrade, replace, and append algorithm elements. The modular structure also provides users with flexible options to bypass (e.g., correction algorithms) and select (e.g., rain rate estimators) specific algorithms or their elements, depending on the user's interests and purpose. This flexibility allowed us to append a new polarimetric algorithm (Seo et al., 2020b) with some additional procedures (e.g., ML layer identification). We evaluate our rainfall estimates generated using the new and former QPE algorithms in Section 4.

Once radar volume data pass the file completeness check in the LDM system, the data processing system takes over and implements several algorithm procedures to generate QPE products. The first step performed in individual radar data processing is data quality control (QC) to eliminate non-meteorological radar returns (e.g., anomalous propagation and ground clutter). In this step, we also filter out noise presented in the radar observables (e.g., differential phase). The QC and other individual radar data processing modules function based on spherical coordinates (e.g., 0.5° by 250 m) and are applied to all elevation angles. After the QC, the system builds temperature soundings within each individual radar domain using the retrieved NWP information and identifies the ML altitude using three-dimensional (3D) spherical coordinates. The system then classifies and assigns precipitation types (e.g., convective and stratiform) on two-dimensional (2D) spherical grids using an approach documented in Seo et al. (2020a). The rain rate estimation module then uses the ML and classification information to apply a suitable estimator to each grid and generates 2D rain rate maps for all elevation angles. The hybrid scan module (e.g.,

Fulton et al., 1999; Seo et al., 2011) combines these multiple elevation maps using a non-parametric kernel function and feeds the final 2D (individual) product into the composite map processing step.

This composite step requires temporal and spatial synchronization since all individual radar maps have different temporal (depending on the radar's volume coverage patterns, or VCP) and spatial coverage. After synchronization, the system generates a composite rain rate map every five minutes and corrects temporal sampling (e.g., radar scanning) errors using the two latest composite maps (Seo and Krajewski, 2015). While the uncorrected instantaneous map is used for map visualization only, the corrected one is fed into a distributed hydrologic model, the Hillslope Link Model (HLM; e.g., Krajewski et al., 2017; Quintero et al., 2020a), for real-time streamflow forecasting. The details of these algorithm modules are provided in Section 3.

2.3 Product visualization

As illustrated in Fig. 3, we visualize instantaneous rain rate and cumulative rain maps for the entire state of Iowa through the Iowa Flood Information System (IFIS, http://ifis.iowafloodcenter.org/ifis/main/). The map interface supports visual selection and flexible navigation for the domain of radars or watersheds of interest using the Google Maps API (e.g., Demir and Krajewski, 2013). This subsystem delivers a new rain rate map to IFIS and offers an animation of these maps for the last six hours. This rain map contains a rain/snow classification, particularly useful in the winter season. This classification uses environmental factors (e.g., atmospheric layer thickness and surface temperature) retrieved from the NWP analysis, and the spatial coverage of snow is overlaid with the rain map as shown in Fig. 3(a). As illustrated in Fig, 3(c), the system also accumulates the rain maps

over time and visualizes daily and cumulative rain maps for up to the last 14 days based to the following steps: (1) today's (cumulative) rain map is generated by accumulating the (temporal sampling) error-corrected rain map once the map is available (e.g., every five minutes) and is reset at midnight; (2) before resetting today's rain map at midnight, it is saved as a daily rain map; and (3) the cumulative rain maps are generated by adding today's map to the aggregation of daily maps over a specified period (e.g., up to 14 days). For faster computation and visualization of cumulative rain maps, the system maintains multi-day aggregation files by adding up daily rain maps and updating them at midnight.

3. Algorithms

In this section, we provide details on scientific algorithms implemented in the data processing subsystem described in Section 2. The processing algorithms are categorized into three groups: (1) NWP analysis processing; (2) individual radar data processing; and (3) composite data processing. Because the system structure and algorithm elements have continuously evolved over time since their initial deployment, we also discuss the changes and advancements of the algorithm components that aim to better represent atmospheric phenomena associated with precipitation microphysics.

3.1 NWP processing

3.1.1 ML identification

The ML is one of the most significant uncertainty factors in radar QPE because most precipitation estimators (e.g., Marshall and Palmer, 1948; Fulton et al., 1998) are based on liquid (rain) drop size distributions (DSDs). As such, estimation accuracy for solid and mixed precipitation within and above the ML tends to be relatively lower than that for

liquid precipitation below the ML. To identify and correct radar observations affected by the ML, many approaches have examined the vertical structure of reflectivity (e.g., Fabry and Zawadzki, 1995) or enhanced DP capabilities (e.g., Baldini and Gorgucci, 2006; Giangrande et al., 2008).

The ML identification module is a new procedure appended to our QPE system in accordance with the recent implementation of a polarimetric QPE algorithm known as specific attenuation (Seo et al., 2020b), which is valid only for liquid precipitation below the ML. Upon the receipt of hourly RAP model analysis in LDM, the module retrieves temperature soundings on the RAP grids within our entire domain. The module refers to a lookup table that assigns a (horizontal) RAP grid to a corresponding radar grid and builds temperature profiles on the spherical coordinates within a radar domain. The module then identifies the ML altitude and flags radar grids below the ML by checking if the temperature at the top of a radar beam at a given location is greater than 5°C. This procedure is applied to all elevation angle data and was tested in Seo et al. (2020a).

3.1.2 Rain/Snow classification

Although many winter precipitation classification algorithms have used radar data (e.g., Park et al., 2009; Thompson et al., 2014), we apply a rather simple scheme that does not depend on radar geometry. Occasionally, the class designation obtained from radar-only algorithms does not agree with the one observed on the ground. This is because of the likely phase changes of precipitation along a falling path between a radar beam elevation and the ground. In our system, we use a classification approach based on the critical thickness (e.g., Keeter and Cline, 1991; Heppner, 1992) and surface temperature together as retrieved from HRRR model analysis with a 3 km horizontal grid. The critical

thickness is defined as the difference of geopotential height between 1,000 and 850 mb. Figure 4 shows the relation between the two variables (e.g., thickness and surface temperature) and precipitation classes observed during the winter seasons in 2012 and 2013. We obtained the observed classes in Fig. 4 from Automated Surface Observing System (ASOS) rain gauges (see Fig. 1), which are equipped with two sensors to detect precipitation classes (e.g., Ramsay, 1997). Based on the preliminary analysis presented in Fig. 4, we selected two thresholds (i.e., 3°C for surface temperature and 1,310 m for the thickness) and applies them to delineate regions with high likelihood of snow. These regions are then overlaid with the instantaneous rain rate map as shown in Fig. 3(a). We note that this snow information is used for qualitative purposes only (e.g., map visualization for weather monitoring) and is not transferred to quantitative (i.e., hydrologic) applications. Because Fig. 4 demonstrates some overlaps (e.g., possible errors) among rain, freezing rain, and snow in the regions near the two threshold values, in Section 5 we discuss this weakness and the probable improvement that could be achieved with a new approach.

3.2 Individual radar data processing

3.2.1 Data quality control (QC)

The QC modules encompass elimination of non-meteorological radar returns and noise filtering of radar observations. While it is comparatively easier to manage anomalous propagation, ground clutter, and biological returns using their polarimetric features (e.g., Ryzhkov and Zrnic, 1998; Rico-Ramirez and Cluckie, 2008), the effects from wind farms (WF) have become a growing challenge (e.g., Vogt et al., 2007). To eliminate the effects from WF and other non-meteorological targets, we previously had used the multiple

thresholds of copular correlation coefficient (ρ_{hv}) conditioned on the reflectivity strength (Seo et al., 2015). However, we found that an aggressive filter (e.g., $\rho_{hv} \geq 0.98$) proposed to handle WF echoes occasionally removes some rain echoes. As such, the current QC module bypasses the aggressive filter and applies a new method instead, which uses vertically integrated liquid water content (VIL) to identify WF echoes (Seo et al., 2020a). The basis of this new idea was the fact that estimated VILs for WF echoes tend to be much lower (e.g., a weaker vertical extension) than those for actual convective cells despite their strong reflectivity contamination.

Unprocessed differential phase (ϕ_{dp}) data require unfolding and smoothing steps (e.g., Wang and Chandrasekar, 2009) because the data are rather noisy and are folded to a limited range (e.g., 0 to 360° for WSR-88D). The noise-filtering module incorporates phase unfolding and smoothing routines used in the WSR-88D Common Operations and Development Environment (CODE) public package (https://www.weather.gov/code88d/). The smoothing routines for ϕ_{dp} processing consist of averaging and median filters. The averaging filter is also applied to horizontal reflectivity (Z), differential reflectivity (Z_{dr}), and ρ_{hv} along a radial direction. The module also derives specific differential phase (K_{dp}) from processed ϕ_{dp} in accordance with the CODE procedure.

3.2.2 Precipitation type and hydrometeor classification

This module splits precipitation into convective and stratiform rain by estimating VIL to define convective cores and gradually expanding the convective area (from the cores to the adjacent grids), based on a region-growing method (e.g., Adams and Bischof, 1994). The VIL estimation using 3D reflectivity and the ML information mitigates the uncertainty associated with the effects of the bright band and radar beam geometry near the radar site

(Seo et al., 2020a). The convective/stratiform classification was originally designed to apply separate rain rate estimators to different rain types, as well as to correct the error arising from the non-uniform vertical profile of reflectivity (VPR) for the stratiform regions (e.g., Bellon et al., 2005; Krajewski et al., 2011). The correction module using a real-time VPR is currently inactive because the default rain rate estimator has been switched from the reflectivity-based method to the specific attenuation method. The real-time VPR correction approach is documented in Seo et al. (2011). We describe both estimators in the next subsection. The module also performs hydrometeor classification for solid and mixed precipitation (e.g., ice and dry/wet snow). This classification uses the polarimetric signatures of Z, Z_{dr}, and ρ_{hv}, described in Straka et al. (2000) and Ryzhkov et al. (2005), combined with ML information. Hail is simply identified when reflectivity is greater than 53 dBZ.

3.2.3 Rain rate estimation

The module provides multiple rain rate (R) estimators, including the new development of specific attenuation (A):

$$R(Z) = 0.017 \cdot Z^{0.714} \tag{1}$$

$$R(Z) = \begin{cases} 0.017 \cdot Z^{0.714} & \text{for convective rain} \\ 0.036 \cdot Z^{0.625} & \text{for stratiform rain} \end{cases} \tag{2}$$

$$R(Z, Z_{dr}) = 0.0067 \cdot Z^{0.927} \cdot Z_{dr}^{-3.43} \tag{3}$$

$$R(K_{dp}) = 40.5 \cdot K_{dp}^{0.85} \tag{4}$$

$$R(A) = 4120 \cdot A^{1.03} \tag{5}$$

where the unit scale of Z and Z_{dr} is decibels (dB) in Eqs. (1), (2), and (3). Although the default rain rate estimator for our QPE system is currently set to specific attenuation using

Eq. (5), such a selective option enables us to investigate the event-dependent performance of the various estimators (e.g., Thurai et al., 2017). While all the estimators presented in Eqs. (1)-(5) are valid only for pure rain below the ML, the module selectively applies one of the estimators in Eq. (6) to solid and mixed precipitation within and above the ML (e.g., Istok et al. 2009):

$$\begin{aligned}
&\text{Wet snow: } 0.6\,R(Z)\\
&\text{Dry snow within the ML: } R(Z)\\
&\text{Dry snow above the top of the ML: } 2.8\,R(Z)\\
&\text{Ice crystals: } 2.8\,R(Z)\\
&\text{Hail: } R(K_{dp}) = 29.0 \cdot K_{dp}^{0.77}
\end{aligned} \tag{6}$$

In the case where the NWP analysis for the ML identification is missing, we simply apply Eq. (1) to the entire radar domain. We note that estimation of specific attenuation A is quite complicated (e.g., Ryzhkov et al., 2014; Wang et al., 2019), and detailed procedures implemented in our QPE algorithm are provided in Seo et al. (2020b).

3.2.4 Hybrid scan

After generating rain rate maps at all elevation angles (e.g., 3D), the hybrid scan module constructs a 2D rain map by vertically combining the 3D rain maps using a linear weighting scheme. A non-parametric kernel function (e.g., log-normal) assigns weights to the elevation data at a given azimuth and range location depending on the vertical distance between the center of the data grid and a predefined constant altitude (e.g., 1.5 km). The total of weights assigned along a vertical column must be unity through the normalization of assigned weights, and the angle data closer to the constant altitude are given greater weight. This smoothing technique tends to mitigate the discontinuity often observed between the transition areas of elevation angles (e.g., Seo et al. 2011). The hybrid scan

approach tends to suppress significant ground clutter caused by the side lobe effect, which occasionally appears in the lowest elevation angle data (e.g., Fulton et al. 1998).

3.2.5 Temporal synchronization

Temporal synchronization of individual rain maps is vital for generating a composite rain product because the observation times and intervals among the radars shown in Fig. 1 differ depending on their local weather conditions. To synchronize all irregular data/map timestamps, we define a five-minute nominal timestamp and generate new rain maps at those timestamps using the latest two consecutive rain maps (see Fig. 2). Our previous synchronization scheme interpolated the two consecutive maps by assigning weights determined by the time separation between the observed maps and the nominal time for which a new map is generated (e.g., Langston et al., 2007). However, we found two weaknesses in this scheme: (1) The interpolation of the same rain system (e.g., a squall line) observed at different times yielded duplicate (or spatially expanded) systems even if the system moved from one place to another; and (2) the timestamp of the interpolated map was always earlier than that of the latest map observed, implying that the latency of a composite map was sometimes up to 15 minutes (because the observed map is labelled by the moment that a radar starts scanning, it already has a delay of 4 to 10 minutes). To resolve these two issues with the interpolation scheme, the current module executes simple tracking of the storm velocity vector using a cross-correlation method (e.g., Fabry et al., 1994; Seo and Krajewski, 2015). This tracking requires grid transformation from radar spherical coordinates to geographic ones. This geographic coordinate system, with a resolution of quarter decimal minutes (equivalent to approximately 0.5 km), also provides a common reference grid for the spatial mosaic of individual rain maps. To accelerate the

tracking computation, the module generates rain maps that are four times coarser and captures the main movement (e.g., single vector), returns to the original grid, and finds the exact vector within an averaging range between the original and coarser scales. The module then projects the estimated vector to the next two timestamps and produces new rain maps (see Fig. 2). This extrapolation assumes that the estimated vector is valid within a projection time domain (e.g., up to 10 minutes).

3.3 Composite data processing

3.3.1 Spatial mosaic

Once the (temporally) synchronized rain maps are ready, the QPE system manager takes over and feeds them into the spatial mosaic process every five minutes. The mosaic module reads the geographic reference points (e.g., upper-left corner) from the map header of all individual rain map files and places the maps onto the common grid. For overlapping areas covered by multiple radars, rainfall values are combined based on a linear weighting scheme using the distance and altitude between the sampling (observation) location and each involved radar site:

$$w_i = \exp\left(-\frac{r_i^2}{R^2}\right) \cdot \exp\left(-\frac{h_i^2}{H^2}\right) \quad (7)$$

where w_i denotes an assigned weight for the i-th radar, and r and h are the distance and altitude (both are in km) between the radar sampling location and the radar sites. R and H represent scale parameters, and a greater (smaller) value for these parameters leads to a gradual (rapid) change of the weight values. We set 100 and 2 km as default values for the distance and altitude scale parameters, respectively. The use of 100 km for the distance parameter smooths the sharp boundaries that occasionally appear in overlapping zones

because of relative calibration biases (e.g., Seo et al., 2013; Keem et al., 2019) between individual radars. The calculated weights for a grid location in the overlapping zone are also normalized to sum up to 1.

3.3.2 Advection correction

It has been recognized that rainfall accumulations using rain rate maps produced from radar's sporadic sampling often result in inaccurate representation (e.g., discontinuous patterns) of actual rain fields (e.g., Huebner et al., 1986; Liu and Krajewski, 1996). This temporal sampling error is often significant, particularly as the storm velocity and the map spatial resolution become faster and higher, respectively. To mitigate this error in the composite rain map, we apply an advection approach using the same vector tracking method as used in the time synchronization module. The advection correction module linearly interpolates static storm locations detected at two consecutive maps and corrects for the missed rainfall accumulations. The module takes two instantaneous composite rain maps with a five-minute interval, calculates and projects a velocity vector, and generates new intermediate rain maps with a one-minute interval within the five-minute domain (Seo and Krajewski, 2015). The module splits the entire spatial domain shown in Fig. 1 into six tiles for faster computation and fulfills the aforementioned advection procedure. An average of the six composite maps (e.g., two originals and four new ones) within the five-minute domain is then delivered to the cumulative process for product visualization and to the hydrologic modeling component for streamflow prediction.

4. Product evaluation

We assess the QPE products generated via the combination of algorithms described in

Section 3 for the three-year period of 2016–2018 in two ways: (1) quantitative comparison with ground reference (i.e., rain gauge) observations; and (2) evaluation of hydrologic simulations driven by the QPE products using streamflow observations. We generated the products using a QPE reproduction system (Seo et al., 2019) that can readily retrieve the radar Level II data from Amazon's cloud archive (e.g., Ansari et al. 2017), with some substantial modifications to append newly-developed processing modules. We acquired rain gauge data from the National Weather Service (NWS) Cooperative Observer Program (COOP; Mosbacher et al. 1989) network and streamflow data from the U.S. Geological Survey (USGS). The domain illustrated in Fig. 1 shows about 220 rain gauge and 140 streamflow stations. The purpose of this evaluation is to demonstrate improvements achieved by our latest algorithms after the recent implementation of the specific attenuation method. We also compare the performance of our QPE products with that of the national QPE products in the United States, Multi-Radar Multi-Sensor (MRMS; Zhang et al., 2016) and NWS Level III Digital Precipitation Rate (DPR). We note that the evaluation analyses are limited to the months of April through October because the quantitative estimation of winter precipitation, both radar- and ground-based, is still challenging.

4.1 Rain gauge evaluation

In this section, we use the daily COOP data to evaluate four QPE products: MRMS, NWSDP, IFC-$R(Z)$, and IFCDP-$R(A)$. "DP" denotes polarimetric estimates. Our LDM has been receiving a set of MRMS QPE products (e.g., radar-only, gauge-corrected, and gauge-only) in real-time; we use the hourly gauge-corrected one in this evaluation. The other three products are radar-only estimates. Concerning NWSDP, we obtained the DPR product for seven WSR-88D radars within the domain shown in Fig. 1 and applied our time

synchronization and spatial mosaic procedures to generate a composite product. As we did not apply our QC and correction modules in NWSDP processing, the primary features of the NWS polarimetric algorithm should be preserved in NWSDP. IFC-$R(Z)$ provides reflectivity-based estimates generated by our former algorithm combination, which does not contain algorithm modules such as noise filtering and ML identification. As such, we estimated IFC-$R(Z)$ using only Eq. (1) for the entire radar domain. The estimation procedure of IFCDP-$R(A)$ is primarily based on the specific attenuation method (Seo et al., 2020b) with the combination of the latest algorithm elements as presented in Section 3.

Figure 5 illustrates the product maps of rain totals accumulated over the month of September 2016. In Fig. 5, we discover that IFC-$R(Z)$ shows an underestimation tendency, while the spatial rainfall structures of the other three products look quite similar. It seems that IFCDP-$R(A)$ effectively manages the partial beam blockage effects, which appear clearly in the southeast direction from the KFSD radar in MRMS, NWSDP, and IFC-$R(Z)$. This is because the specific attenuation method is known to be less sensitive to radar miscalibration, partial beam blockage, and the variability of DSDs (e.g., Ryzhkov et al., 2014; Wang et al., 2019). We observed many isolated spikes in NWSDP, which correspond to WF in Iowa and Minnesota (for exact WF locations, see Seo et al., 2020a). These spikes indicate that the NWS algorithm has a QC issue, and several spikes near the border between Iowa and Minnesota are also detected in MRMS. In Figs. 6 and 7, we present the quantitative evaluation results for the four products using the independent COOP gauge data at daily and yearly (April to October) scales with three statistical metrics: multiplicative bias (B) defined as a radar–gauge ratio (R/G); Pearson correlation coefficient (r); and mean absolute error (MAE). The term "independent" indicates that the data from

the Hydrometeorological Automated Data System (e.g., Kim et al., 2009) included in the MRMS gauge correction procedure were not involved in this evaluation. As shown in Fig. 6, the dots representing MRMS, NWSDP, and IFCDP-$R(A)$ tend to align along the one-to-one line with somewhat different degrees of scatter. IFC-$R(Z)$ shows the largest scatter, as well as inconsistent bias changes from year to year. IFCDP-$R(A)$, a radar-only product, shows performance (e.g., accuracy) quite comparable to MRMS, which contains a bias correction based on rain gauge observations. NWSDP also provides good estimates, except for an underestimation observed in 2018 and somewhat larger dispersion when compared to MRMS and IFCDP-$R(A)$. The daily evaluation results, represented as 2D histograms, are provided in Fig. 7. The observed degrees of overall bias and dispersion for each QPE product shown in Fig. 6 are consistent with those displayed in Fig. 7. Figure 7 also reveals that the four products are characterized by different uncertainty features conditioned on rainfall magnitude.

4.2 Hydrologic evaluation

The hillslope link model (HLM) is a fully distributed hydrologic model that currently provides real-time streamflow predictions for the entire Iowa domain (Krajewski et al. 2017; Quintero et al. 2020a,b). The HLM is based on landscape decomposition into hillslopes and channel links, which enables the physical representation of runoff generation and water transport. The HLM is calibration-free: its parameters are determined a priori; therefore, the model does not "favor" any specific forcing inputs. Further details regarding the HLM equations, configuration, and numerical solver are documented in earlier studies (e.g., Small et al., 2013; Quintero et al., 2016; Krajewski et al., 2017; Quintero et al., 2020a).

We ran HLM using the hourly MRMS, IFC-$R(Z)$, and IFCDP-$R(A)$ products as model forcing inputs and generated streamflow simulations at a 15-minute time interval. We excluded NWSDP from the model forcing stream because of its erroneous features (e.g., strong spikes and unknown radial patterns shown in Fig. 5). The HLM simulations driven by different forcing products for each year started with the same initial condition (e.g., model state on April 1) captured from the MRMS–HLM run for an antecedent period. We did not calibrate model parameters because model calibration may obscure forcing-dependent differences in streamflow generation.

For a hydrologic evaluation of the different QPE forcing products, we use the performance metrics of Kling-Gupta efficiency (KGE; Gupta et al., 2009), Pearson correlation coefficient (r), MAE, and root mean square error (RMSE). KGE describes the predictive power of hydrologic models and addresses deficiencies in Nash-Sutcliffe efficiency (NSE; Nash and Sutcliff 1970). Figure 8 shows a direct comparison of the effects on performance (represented by KGE) derived from different forcing products. In Fig. 8, hydrologic simulation results driven by IFCDP-$R(A)$ are compared with those driven by IFC-$R(Z)$ and MRMS at about 140 USGS stations in Iowa. For the years 2016 and 2017, IFCDP-$R(A)$ outperforms IFC-$R(Z)$, and the performance of IFCDP-$R(A)$ looks comparable with that of the reference QPE product (MRMS), similar to Fig. 6. Although MRMS seems slightly better than IFCDP-$R(A)$ for 2018, KGE differences between the two products are likely not significant at a KGE range of about 0.3–0.7 (e.g., a cluster of dots slightly above the one-to-one line at the KGE range). To further examine the performance of MRMS and IFCDP-$R(A)$, we compare the results from both forcing products regarding catchment scale (e.g., upstream basin areas of the USGS stations) in Fig. 9. On average,

the performance based on all four metrics tends to be better for both forcing products as the catchment scale becomes larger. Performance varies from year to year, and no QPE product (MRMS or IFCDP-$R(A)$) is consistently better.

5. Summary and discussion

In this paper, we document the architecture, algorithm configuration, and estimation performance of our real-time QPE system used primarily for flood prediction in Iowa. The IFC system is the only academia-based large-scale (statewide) real-time radar-rainfall monitoring system in the United States. The system retrieves data from operational radars and NWP models and uses a variety of scientific algorithms to account for precipitation microphysics and uncertainties in radar remote sensing (e.g., Villarini and Krajewski, 2010). NWP analysis (e.g., temperature and geopotential height) acquired through LDM facilitates the ML identification and rain/snow classification. Real-time streaming data transferred from individual radars undergo several sequential processing procedures before they are combined into a composite product that covers the entire Iowa domain (Fig. 1). This sequential processing includes the radar data QC (removal of non-meteorological echoes and noise filtering), precipitation type and hydrometeor classification, rain rate estimation, hybrid scan construction, and time synchronization of individual rain maps. The composite processing modules then spatially combine the synchronized rain maps and correct for the error arising from the radar's periodic temporal sampling. Finally, the (composite) instantaneous and accumulated rain maps are visualized through IFIS (e.g., Krajewski et al., 2017), a flood information portal open to the general public. These statewide rain maps are updated every five minutes, implying that all individual and composite data processing procedures are done within a five-minute window.

The key feature of our QPE system is its flexible system structure (e.g., modular configuration), which allows us to improve its utility and performance by upgrading and appending algorithm elements. One notable example is the recent implementation of new polarimetric algorithms while maintaining the main system structure and existing algorithm modules. The new polarimetric algorithms include the precipitation estimators presented in Eqs. (3)-(5) and several subject elements, such as noise filtering and ML identification procedures. The specific attenuation method is a default estimator in our current operation and has improved the estimation accuracy significantly, compared to the former one based on a conventional *Z-R* relation (Seo et al., 2020b). We have demonstrated that our composite specific attenuation estimates are more reliable and robust with regard to the variability of DSDs and partial beam blockage, and their performance (e.g., accuracy) is comparable with MRMS, which relies on a gauge correction (Fig. 6). We have also verified that QPE improvements achieved through this new implementation lead to better simulation of streamflow (Fig. 8).

The next module element we plan to update (or replace) is the rain/snow classification because the current threshold scheme has revealed many cases of misclassification (see e.g., Fig. 4). Data-driven approaches (e.g., machine learning) will likely be useful to inspect the multi-dimensional features of many more variables (e.g., thickness, temperature, web-bulb temperature, relative humidity, and radar observations) relevant to winter precipitation processes. Bringing radar observations into this classification framework will also enable a rapid map update; the rain/snow boundary in the current one stays static for an hour based on the NWP's update cycle.

While we have demonstrated our algorithm's application to a limited spatial domain

(i.e., Iowa), the framework described in this paper is transferrable to other geographic areas and expandable to a larger (e.g., regional) scale. The new estimator (e.g., specific attenuation) in our QPE system should be more robust through this transition because its estimates are less sensitive to the variability of DSDs (e.g., Ryzhkov et al., 2014), which could vary considerably in different geographic regions. The required resources for the domain change include radar information (e.g., ID, geographic location, and spatial coverage) and lookup tables for grid matching between the individual radar and NWP domains. Our experience with the successful application of prior developments (e.g., Krajewski et al., 2013) to different regions of the United States (e.g., Lin et al., 2010; Yang et al., 2014) confirms the system's flexibility with regard to domain change and expansion. We are planning to expand the system to a much larger domain including neighboring states (e.g., Kansas, Missouri, and Nebraska) for the purpose of flood mitigation in the Mississippi and the Missouri river basins. We hope to report the results and discuss the challenging aspects of the domain expansion soon.

Acknowledgments: The Iowa Flood Center at the University of Iowa supported this work. The evaluation of various QPE products was partially supported by the NOAA Hydrometeorology Testbed (HMT) Program within NOAA/OAR Office of Weather and Air Quality under Grant NA17OAR4590131. Thanks to Dr. Felipe Quintero at the Iowa Flood Center for providing the HLM simulation results driven by the different QPE products for the hydrologic evaluations in this project.

References

Adams, R., Bischof, L., 1994. Seeded region growing. IEEE T. Pattern Anal. 16, 641–647.

Ansari, S., Greco, S.D., Kearns, E., Brown, O., Wilkins, S., Ramamurthy, M., Weber, J., May, R., Sundwall, J., Layton, J., Gold, A., Pasch, A., Lakshmanan, V., 2017. Unlocking the potential of NEXRAD data through NOAA's big data partnership. Bull. Am. Meteorol. Soc. 99, 189–204.

Baldini, L., Gorgucci, E., 2006. Identification of the melting layer through dual-polarization radar measurements at vertical incidence. J. Atmos. Oceanic Technol. 23, 829–839.

Bellon, A., Lee, G. Zawadzki, I., 2005. Error statistics of VPR corrections in stratiform precipitation. J. Appl. Meteorol. 44, 998–1015.

Benjamin, S.G., Weygandt, S.S., Brown, J.M., Hu, M., Alexander C.R., Smirnova, T.G., Olson, J.B., James, E.P., Dowell, D.C., Grell, G.A., Lin H., Peckham, S.E., Smith, T.L., Moninger, W.R., Kenyon, J.S., Manikin, G.S., 2016. A North American hourly assimilation and model forecast cycle: The Rapid Refresh. Mon. Wea. Rev. 144, 1669–1694.

Crum, T.D., Alberty, R.L., Burgess, D.W., 1993. Recording, archiving, and using WSR-88D data. Bull. Am. Meteorol. Soc. 74, 645–653.

Cunha, L.K., Smith, J.A., Baeck, M.L., Krajewski, W.F., 2013. An early performance evaluation of the NEXRAD dual-polarization radar rainfall estimates for urban flood applications. Weather. Forecast. 28, 1478–1497.

Demir, I., Krajewski, W.F., 2013. Towards an integrated flood information system: Centralized data access, analysis, and visualization. Environ. Modell. Softw. 50, 77–84.

Fabry, F., Bellon, A., Duncan, M.R., Austin, G.L., 1994. High resolution rainfall measurements by radar for very small basins: The sampling problem re-examined. J. Hydrol. 161, 415–428.

Fabry, F., Zawadzki, I., 1995. Long term observations of the melting layer of precipitation and their interpretation. J. Atmos. Sci., 52, 838–851.

Fulker, D., Bates, S., Jacobs, C., 1997. Unidata: A virtual community sharing resources via technological infrastructure. Bull. Am. Meteorol. Soc. 78, 457–468.

Fulton, R.A., Breidenbach, J.P., Seo, D.-J., Miller, D.A., O'Bannon, T., 1998. The WSR-88D rainfall algorithm. Weather Forecast. 13, 377–395.

Giangrande, S.E., Krause, J.M., Ryzhkov, A.V., 2008. Automatic designation of the melting layer with a polarimetric prototype of the WSR-88D radar. J. Appl. Meteor. Climatol. 47, 1354–1364.

Gupta, H.V., Kling, H., Yilmaz, K.K., Martinez, G.F., 2009. Decomposition of the mean squared error and NSE performance criteria: Implications for improving hydrological modelling. J. Hydrol. 377, 80–91.

Heppner, P.O.G., 1992. Snow versus rain: Looking beyond the "magic" numbers. Weather Forecast. 7, 683–691.

Huebner, G.L., Zdenek, D.J., Fornear, J.L., 1986. Sampling interval and area effects on radar-derived rainfall estimates. Preprints, 23rd Conf. on Radar Meteorology and Cloud Physics, Snowmass, CO, Amer. Meteor. Soc., 22–26.

Istok, M.J., Fresch, M., Jing, Z., Smith, S.D., Murnan, R., Ryzhkov, A., Krause, J., Jain, M., Schlatter, P., Ferree, J., Klein, B.R., Stein, D., Cate, G., Saffle, R.E., 2009. WSR-88D dual-polarization initial operational capabilities. Preprints, 25th Conf. on Int. Interactive Information and Processing Systems (IIPS) in Meteorology, Oceanography, and Hydrology, Phoenix, AZ, Amer. Meteor. Soc., 15.5.

Keem, M., Seo, B.-C., Krajewski, W.F., Morris, K.R., 2019. Inter-comparison of reflectivity measurements between GPM DPR and NEXRAD Radars. Atmos. Res. 226, 49–65.

Keeter, K.K., Cline, J.W., 1991. The objective use of observed and forecast thickness values to predict precipitation type in North Carolina. Weather Forecast. 6, 456–469.

Kelleher, K.E., Droegemeier, K.K., Levit, J.J., Sinclair, C., Jahn, D.E., Hill, S.D., Mueller, L., Qualley, G., Crum, T.D., Smith, S.D., Del Greco, S.A., Lakshmivarahan, S., Miller, L., Ramamurthy, M., Domenic, B., Fulker, D.W., 2007. A real-time delivery system for NEXRAD Level II data via the internet. Bull. Am. Meteorol. Soc. 88, 1045–1057.

Kim, D., Nelson, B., Seo, D.J., 2009. Characteristics of reprocessed Hydrometeorological Automated Data System (HADS) hourly precipitation data. Weather Forecast. 24, 1287–1296

Krajewski, W.F., Ceynar, D., Demir, I., Goska, R., Kruger, A., Langel, C., Mantilla, R.,

Niemeier, J., Quintero, F., Seo, B.-C., Small, S., Weber, L., Young, N., 2017. Real-time flood forecasting and information system for the State of Iowa. Bull. Am. Meteorol. Soc. 98, 539–554.

Krajewski, W.F., Kruger, A., Singh, S., Seo, B.-C., Smith, J.A., 2013. Hydro-NEXRAD-2: Real-time access to customized radar-rainfall for hydrologic applications. J. Hydroinform. 15, 580–590.

Krajewski, W.F., Kruger, A., Smith, J.A., Lawrence, R., Gunyon, C., Goska, R., Seo, B.-C., Domaszczynski, P., Baeck , M.L., Ramamurthy, M.K., Weber, J., Bradley, A.A., DelGreco, S.A., Steiner, M., 2011. Towards better utilization of NEXRAD data in hydrology: An overview of Hydro-NEXRAD. J. Hydroinform. 13, 255–266.

Krajewski, W.F., Vignal, B., Seo, B.-C., Villarini, G., 2011. Statistical model of the range-dependent error in radar-rainfall estimates due to the vertical profile of reflectivity. J. Hydrol. 402, 306–316.

Kruger, A., Krajewski, W.F., Domaszczynski, P., Smith, J.A., 2011. Hydro-NEXRAD: Metadata computation and use. J. Hydroinform. 13, 267–276.

Langston, C., Zhang, J., Howard, K., 2007. Four-dimensional dynamic radar mosaic. J. Atmos. Oceanic Technol. 24, 776–790.

Lin, N., Smith, J.A., Villarini, G., Marchok, T.P., Baeck, M.L., 2010. Modeling extreme rainfall, winds, and surge from Hurricane Isabel (2003). Weather Forecast. 25, 1342–1361.

Liu, C., Krajewski, W.F., 1996. A comparison of methods for calculation of radar-rainfall hourly accumulations. Water Resour. Bulllr. 32, 305–315.

Marshall, J.S., Palmer, W.M.K., 1948. The distribution of raindrops with size. J. Appl. Meteorol. 5, 165–166.

Mosbacher, R., Evans, W.E., Friday, E.W. Jr., 1989. Cooperative station observations, National Weather Service Observing Handbook No. 2, Silver Spring, Maryland.

Nash, J.E., Sutcliffe, J.V., 1970. River flow forecasting through conceptual models. part I–A discussion of principles. J. Hydrol. 10, 282–290.

Park, H., Ryzhkov, A.V., Zrnić, D.S., Kim, K.E., 2009. The hydrometeor classification algorithm for the polarimetric WSR-88D: Description and application to an MCS. Weather. Forecast. 24, 730–748.

Quintero, F., Krajewski, W.F., Mantilla, R., Small, S., Seo, B.-C., 2016. A spatial-dynamical framework for evaluation of satellite rainfall products for flood prediction. J. Hydrometeor. 17, 2137–2154.

Quintero, F., Krajewski, W.F., Seo, B.-C., Mantilla, R., 2020a. Improvement and evaluation of the Iowa Flood Center Hillslope Link Model (HLM) by calibration-free approach. J. Hydrol. 584, 124686.

Quintero, F., Rojas, M., Krajewski, W.F., 2020b. A flood potential index for effective communication of streamflow forecasts at ungauged communities. J. Hydrometeor. (in press)

Ramsay, A.C., 1997. Freezing rain detection and reporting by the automated surface observing system (ASOS). Proceedings of the First Symposium on Integrated Observing Systems and 7th Conference on Aviation, Range, and Aerospace Meteorology, Long Beach, CA. Amer. Meteor. Soc., pp. J65–J78.

Rico-Ramirez, M.A., Cluckie, I.D., 2008. Classification of ground clutter and anomalous propagation using dual-polarization weather radar. IEEE Trans. Geosci. Remote. Sens. 46, 1892–1904.

Ryzhkov, A., Diederich, M., Zhang, P., Simmer, C., 2014. Potential utilization of specific attenuation for rainfall estimation, mitigation of partial beam blockage, and radar networking. J. Atmos. Oceanic Technol. 31, 599–619.

Ryzhkov, A.V., Schuur, T.J., Burgess, D.W., Heinselman, P.L., Giangrande, S.E., Zrnic, D.S., 2005. The joint polarization experiment: Polarimetric rainfall measurements and hydrometeor classification. Bull. Am. Meteorol. Soc. 86, 809–824.

Ryzhkov, A.V., Zrnic, D.S., 1998. Polarimetric rainfall estimation in the presence of anomalous propagation. J. Atmos. Oceanic Technol. 15, 1320–1330.

Seo, B.-C., Cunha, L.K., Krajewski, W.F., 2013. Uncertainty in radar-rainfall composite and its impact on hydrologic prediction for the eastern Iowa flood of 2008. Water Resour. Res. 49, 2747–2764.

Seo, B.-C., Keem, M., Hammond, R., Demir, I., Krajewski, W.F., 2019. A pilot infrastructure for searching rainfall metadata and generating rainfall product using the big data of NEXRAD. Environ. Modell. Softw. 117, 69–75.

Seo, B.-C., Krajewski, W.F., 2015. Correcting temporal sampling error in radar-rainfall:

Effect of advection parameters and rain storm characteristics on the correction accuracy. J. Hydrol. 531, 272–283.

Seo, B.-C., Krajewski, W.F., Kruger, A., Domaszczynski, P., Smith, J.A., Steiner, M., 2011. Radar-rainfall estimation algorithms of Hydro-NEXRAD. J. Hydroinform. 13, 277–291.

Seo, B.-C., Krajewski, W.F., Mishra, K.V., 2015. Using the new dual-polarimetric capability of WSR-88D to eliminate anomalous propagation and wind turbine effects in radar-rainfall. Atmos. Res. 153, 296–309.

Seo, B.-C., Krajewski, W.F., Qi, Y., 2020a. Utility of vertically integrated liquid water content for radar-rainfall estimation: Quality control and rain type classification. Atmos. Res. 236, 104800.

Seo, B.-C., Krajewski, W.F., Quintero, F., ElSaadani, M., Goska, R., Cunha, L.K., Dolan, B., Wolff, D.B., Smith, J.A., Rutledge, S.A., Petersen, W.A., 2018. Comprehensive evaluation of the IFloodS radar-rainfall products for hydrologic applications. J. Hydrometeor. 19, 1793–1813.

Seo, B.-C., Krajewski, W.F., Ryzhkov, A., 2020b. Evaluation of the specific attenuation method for radar-based quantitative precipitation estimation: Improvements and practical challenges. J. Hydrometeor. 21, 1333–1347.

Small, S.J., Jay, L.O., Mantilla, R., Curtu, R., Cunha, L.K., Fonley, M., Krajewski, W.F., 2013. An asynchronous solver for systems of ODEs linked by a directed tree structure. Adv. Water Resour. 53, 23–32.

Smith, J.A., Baeck, M.L., Villarini, G., Wright, D.B., Krajewski, W., 2013. Extreme flood response: The June 2008 flooding in Iowa. J. Hydrometeorol. 14, 1810–1825.

Straka, J.M., Zrnić, D.S., Ryzhkov, A.V., 2000. Bulk hydrometeor classification and quantification using polarimetric radar data: Synthesis of relations. J. Appl. Meteorol. Clim. 39, 1341–1372.

Thompson, E., Rutledge, S., Dolan, B., Chandrasekar, V., 2014. A dual polarimetric radar hydrometeor classification algorithm for winter precipitation. J. Atmos. Ocean. Technol. 31, 1457–1481.

Thurai, M., Mishra, K.V., Bringi, V.N., Krajewski, W.F., 2017. Initial results of a new composite-weighted algorithm for dual-polarized X-band rainfall estimation. J.

Hydrometeor. 18, 1081–1100.

Vennapusa, P.K.R., White, D.J., 2015. Performance assessment of secondary-roadway infrastructure in Iowa after 2011 Missouri River flooding. J. Infrastruct. Syst. 21, 10.1061/(ASCE)IS.1943-555X.0000255, 05015003.

Villarini, G., Krajewski, W.F., 2010. Review of the different sources of uncertainty in single polarization radar-based estimates of rainfall. Surv. Geophys. 31, 107–129.

Vogt, R.J., Reed, J., Crum, T., Snow, J.T., Palmer, R.D., Isom, B.M., Burgess, D.W., 2007. Impacts of wind farms on WSR-88D operations and policy considerations. Preprints, 23rd Int. Conf. on Interactive Information Processing Systems (IIPS) for Meteorology, Oceanography, and Hydrology, San Antonio, TX. Amer. Meteor. Soc. 5B.7.

Wang, Y., Chandrasekar, V., 2009. Algorithm for estimation of the specific differential phase J. Atmos. Ocean. Technol. 26, 2565–2578.

Wang, Y., Cocks, S., Tang, L., Ryzhkov, A., Zhang, P., Zhang, J., Howard, K., 2019. A prototype quantitative precipitation estimation algorithm for operational S-band polarimetric radar utilizing specific attenuation and specific differential phase. Part I: Algorithm description. J. Hydrometeor. 20, 985–997.

Weygandt, S., Smirnova, T., Benjamin, S., Brundage, K., Sahm, S., Alexander, C., Schwartz, B., 2009. The High Resolution Rapid Refresh (HRRR): An hourly updated convection resolving model utilizing radar reflectivity assimilation from the RUC/RR. 23rd Conf. on Weather Analysis and Forecasting/19th Conf. on Numerical Weather Prediction, Omaha, NE, Amer. Meteor. Soc., 15A.6. [Available online at https://ams.confex.com/ams/23WAF19NWP /techprogram/paper_154317.htm.]

Yang, L., Smith J.A., Baeck, M.L., Bou-Zeid, E., Jessup, S.M., Tian, F., Hu, H., 2014. Impact of urbanization on heavy convective precipitation under strong large-scale forcing: A case study over the Milwaukee–Lake Michigan region. J. Hydrometeor. 15, 261–278.

Yoksas, T., Emmerson, S., Chiswell, S., Schmidt, M., Stokes, J., 2006. The Unidata Internet Data Distribution (IDD) system: A decade of development. 22nd Int. Conf. on Interactive Information and Processing Systems for Meteorology, Oceanography, and Hydrology, Atlanta, GA, Amer. Meteor. Soc., 6.4. [Available online at https://ams.confex.com/ams/pdfpapers/105113.pdf.]

Zhang, J., Howard, K., Langston, C., Kaney, B., Qi, Y., Tang, L., Grams, H., Wang, Y., Cocks, S., Martinaitis, S., Arthur, A., Cooper, K., Brogden, J., Kitzmiller, D., 2016. Multi-Radar Multi-Sensor (MRMS) quantitative precipitation estimation: initial operating capabilities. Bull. Am. Meteorol. Soc. 97, 621–638.

List of Figures

Fig. 7. The same evaluation as Fig. 6 (using the same QPE products and rain gauge data) but at the daily scale. Results are represented as 2D histograms. A specific color designates the number of occurrences for given gauge and radar rainfall values.

Fig. 8. Comparisons of hydrologic performance driven by IFCDP-$R(A)$ with that driven by IFC-$R(Z)$ and MRMS. The dots in each plot indicate the KGE values at about 140 USGS stations in Iowa.

Fig. 9. Four performance metrics (correlation, MAE, RMSE, and KGE) obtained from hydrologic simulations driven by MRMS and IFCDP-$R(A)$ regarding catchment scale. RMSE values were normalized by the mean annual streamflow discharge at each USGS station.

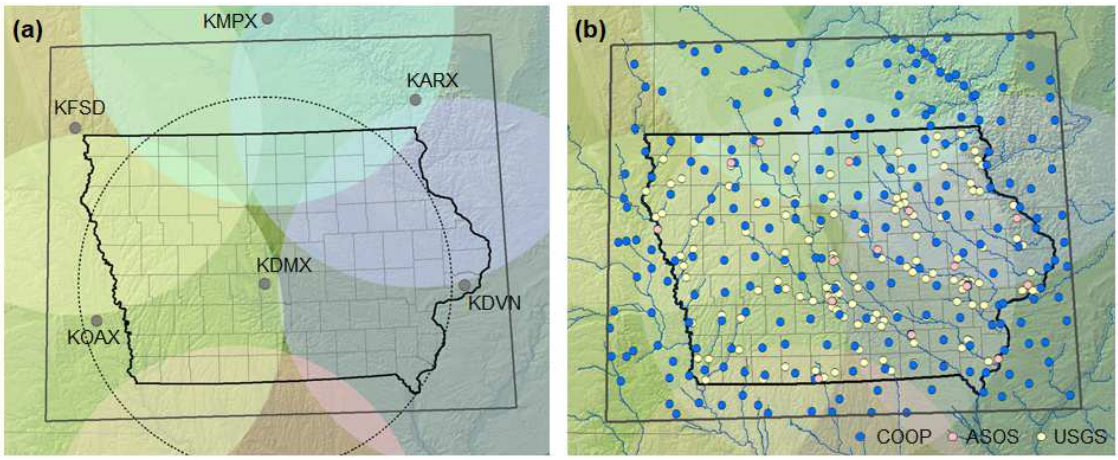

Fig. 1. The QPE system spatial coverage with (a) the involved radar locations and (b) the reference rain (COOP and ASOS) and stream (USGS) gauge locations for its product evaluation. The KEAX radar in Kansas City, Missouri is not shown in (a). The black solid line and gray box represent the Iowa border and IFC domain extent for the QPE product generation, respectively. The circular dashed line and colored areas centered on individual radars indicate their 230 km coverage. The blue solid lines in (b) denote major rivers and streams in the domain.

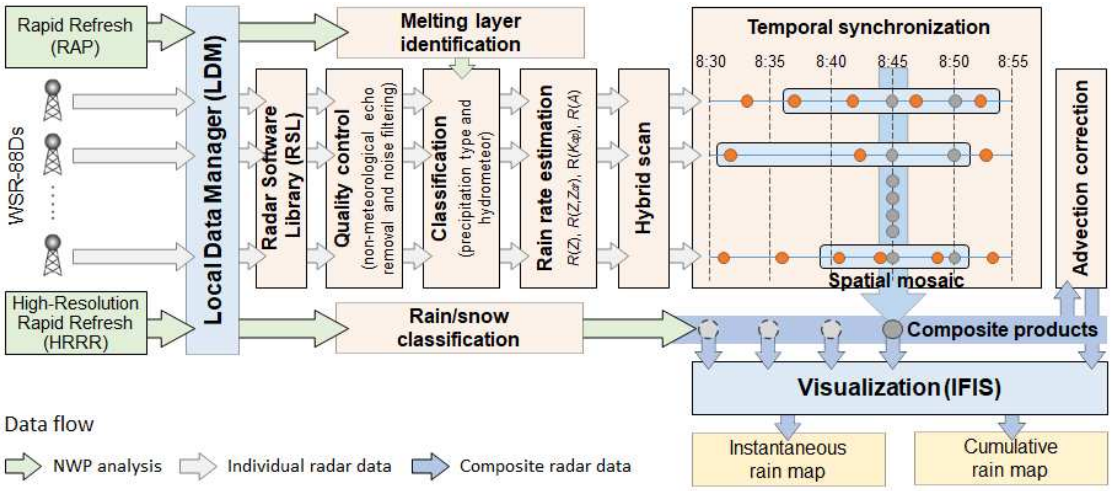

Fig. 2. Overall system architecture illustrating the NWP analysis and radar data flow and sequential processing procedures.

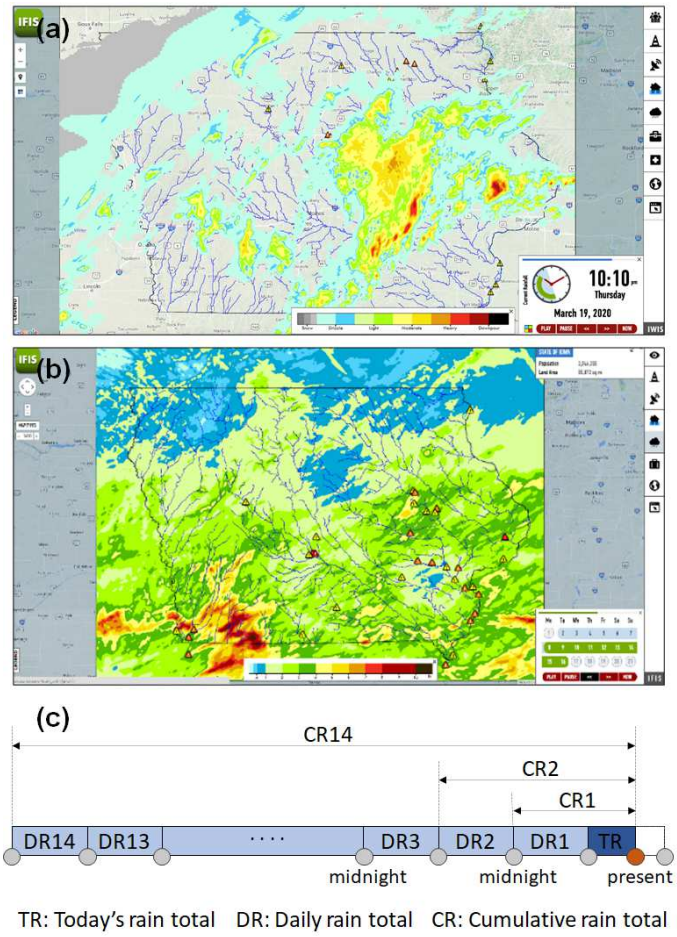

Fig. 3. Examples of real-time rainfall product maps visualized in IFIS: (a) an instantaneous rain rate map with snow (gray) area identification; and (b) a cumulative rain map. The temporal range of daily (DR) and cumulative (CR) rain maps is defined in (c).

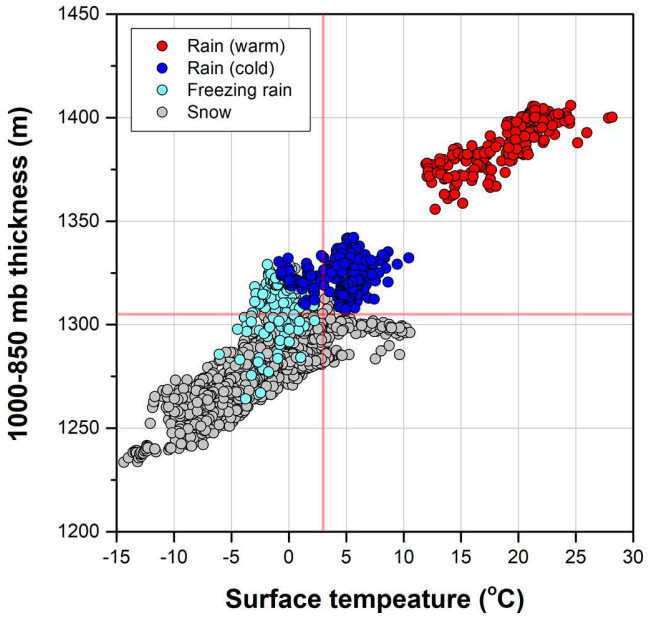

Fig. 4. Precipitation classes characterized by the surface temperature and critical thickness (1000-850 mb) retrieved from the NWP model (e.g., HRRR). The precipitation classes (rain, freezing rain, and snow) were observed at the ground using the ASOS stations in Iowa. The red lines indicate the thresholds used in our rain/snow classification.

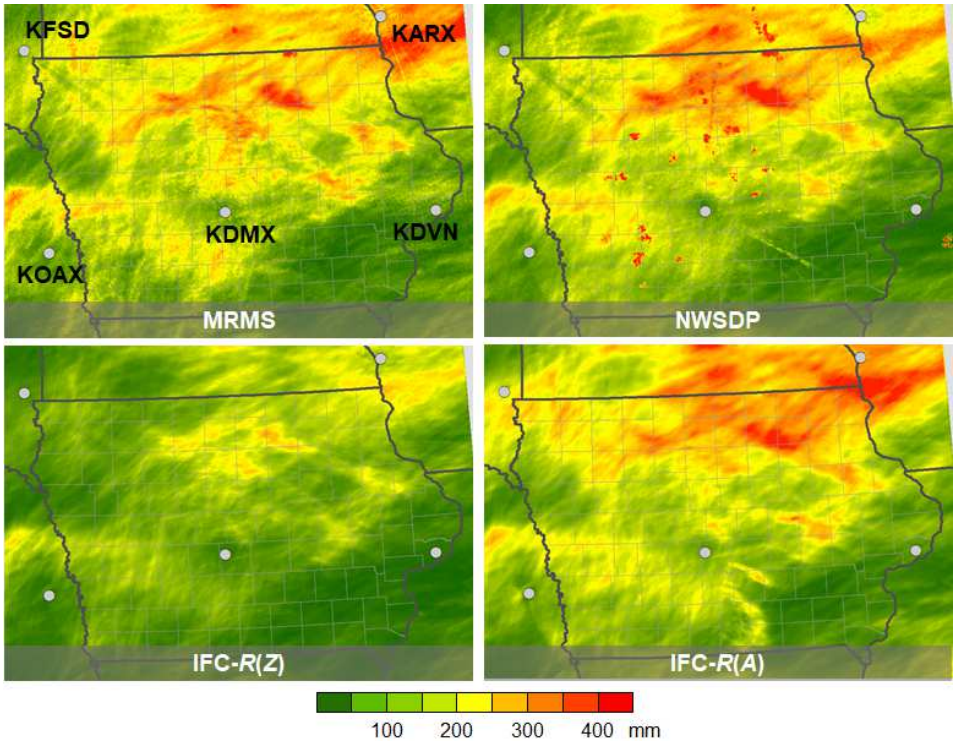

Fig. 5. Maps of one-month rain totals (September 2016) for the MRMS, NWSDP, IFC-*R*(*Z*), and IFC-*R*(*A*) products.

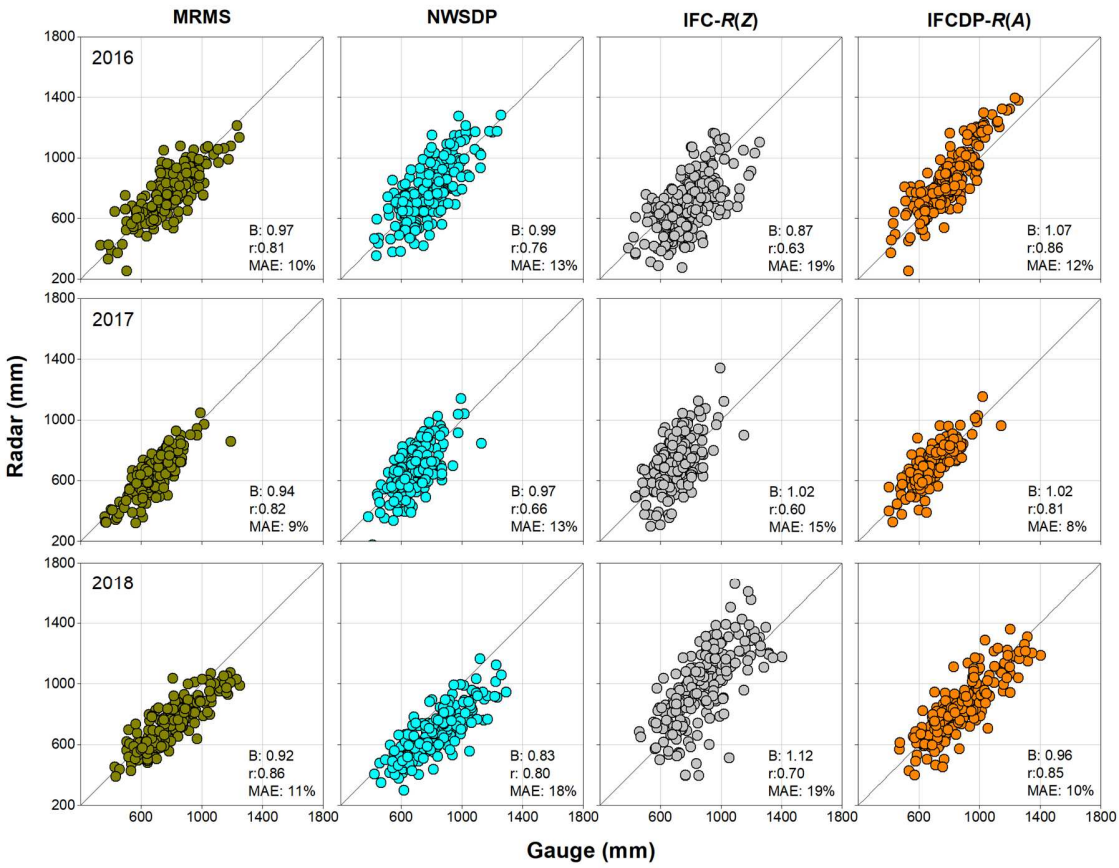

Fig. 6. Quantitative evaluation of the MRMS, NWSDP, IFC-*R*(*Z*), and IFC-*R*(*A*) products using rain gauge (COOP) data at annual (April to October) total scale. Three performance metrics (bias, correlation, and MAE) are provided in each scatter plot. The MAE values were normalized by the gauge mean and presented as percentages.

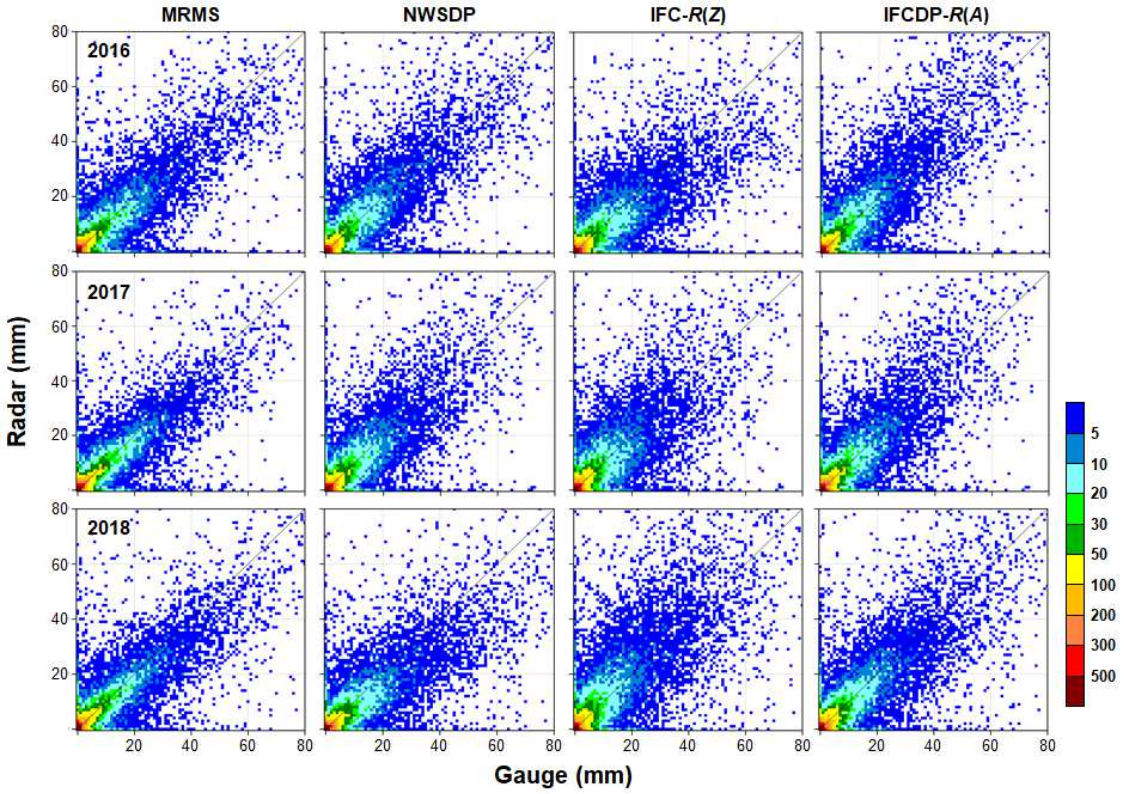

Fig. 7. The same evaluation as Fig. 6 (using the same QPE products and rain gauge data) but at the daily scale. Results are represented as 2D histograms. A specific color designates the number of occurrences for given gauge and radar rainfall values.

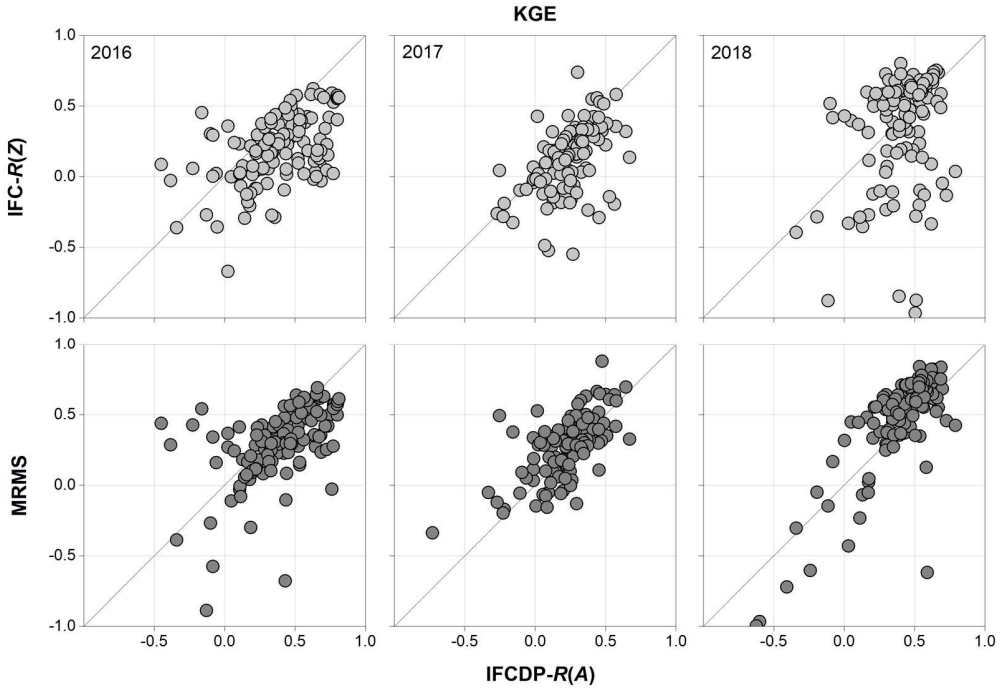

Fig. 8. Comparisons of hydrologic performance driven by IFCDP-*R*(*A*) with that driven by IFC-*R*(*Z*) and MRMS. The dots in each plot indicate the KGE values at about 140 USGS stations in Iowa.

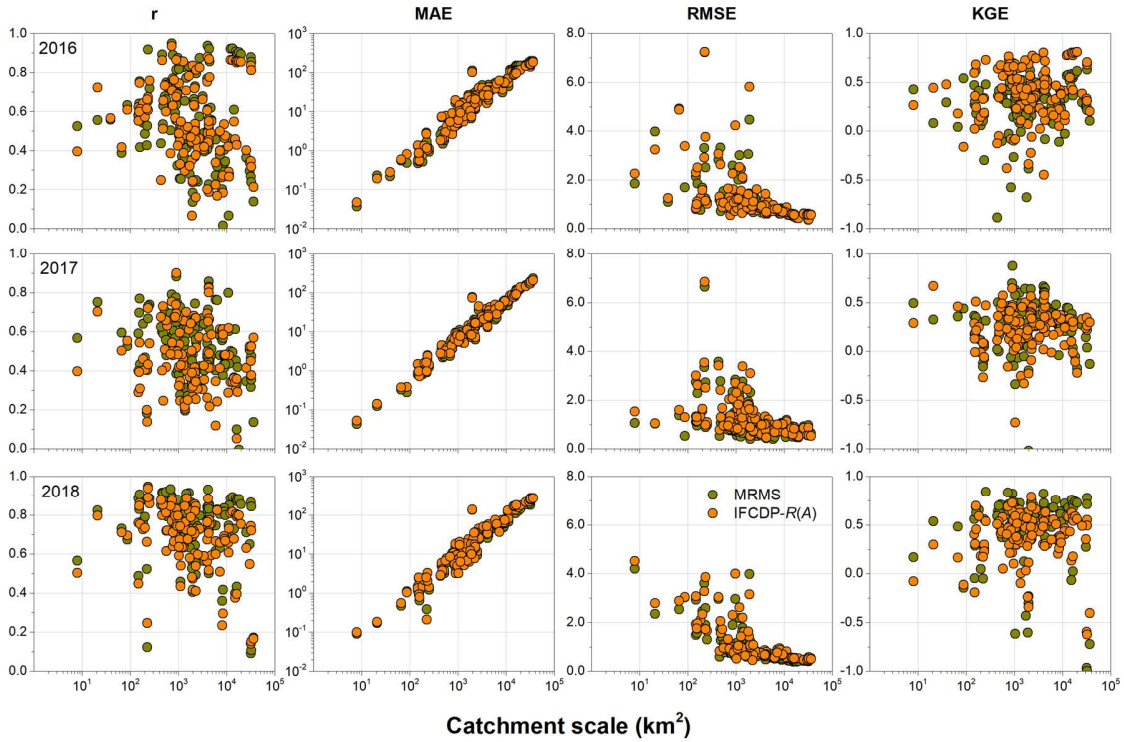

Fig. 9. Four performance metrics (correlation, MAE, RMSE, and KGE) obtained from hydrologic simulations driven by MRMS and IFCDP-*R*(*A*) regarding catchment scale. RMSE values were normalized by the mean annual streamflow discharge at each USGS station.